

Predictive transport simulations of internal transport barriers using the Multi-Mode model

P. Zhu,^{a)} G. Bateman, A. H. Kritz, and W. Horton^{a)}

Physics Department, Lehigh University, 16 Memorial Drive East, Bethlehem, Pennsylvania 18015

(Received 14 February 2000; accepted 23 March 2000)

The formation of internal transport barriers observed in both Joint European Torus (JET) [P. H. Rebut, R. J. Bickerton, and B. E. Keen, *Nucl. Fusion* **25**, 1011 (1985)] and Doublet III-D Tokamak (DIII-D) [J. L. Luxon and L. G. Davis, *Fusion Technol.* **8**, 441 (1985)] are reproduced in predictive transport simulations. These simulations are carried out for two JET-optimized shear discharges and two DIII-D negative central shear discharges using the Multi-Mode model in the time-dependent 1-1/2-D BALDUR transport code [C. E. Singer *et al.*, *Comput. Phys. Commun.* **49**, 275 (1988)]. The Weiland model is used for drift modes in the Multi-Mode model in combination with either Hahn–Burrell or Hamaguchi–Horton flow shear stabilization mechanisms, where the radial electric field is inferred from the measured toroidal velocity profile and the poloidal velocity profile computed using neoclassical theory. The transport barriers are apparent in both the ion temperature and thermal diffusivity profiles of the simulations. The timing and location of the internal transport barriers in the simulations and experimental data for the DIII-D cases are in good agreement, though some differences remain for the JET discharges. The formations of internal transport barriers are interpreted as resulting from a combination of $\mathbf{E} \times \mathbf{B}$ flow shear and weak magnetic shear mechanisms. © 2000 American Institute of Physics. [S1070-664X(00)04107-0]

I. INTRODUCTION

Internal transport barriers (ITBs) have now been observed in most large tokamaks^{1–6} since they were first discovered in the Japan Atomic Energy Research Institute Tokamak-60 Upgrade (JT-60U).^{7,1,2} An ITB is a region where a steep temperature and/or density gradient forms inside a tokamak plasma, usually within the region $\rho \leq 0.6$, where ρ is the normalized minor radius. In tokamaks with toroidal plasma velocity measurements, it is found that the region within an ITB is also the region where the toroidal rotation velocity gradient is steep. This high-performance regime can occur with a lower power threshold than required for the high confinement mode (H-mode) regime, where the transport barriers are located at the plasma edge.

Internal transport barriers are produced in two optimized magnetic shear (OS) discharges in the Joint European Torus (JET),⁸ shot #40542 and #40847.^{5,6,9} In both shots, neutral beam injection (NBI) is the major auxiliary power source, although there is some rf heating as well. The q profiles generated by current ramping in these two shots are flat and low in the core (near the magnetic axis) and steeply rising approaching the edge, with the minimum value of q greater than unity throughout the plasma. In both discharges, the ITB forms first in the core while the edge remains in the low confinement mode (L-mode). Then, the ITB expands towards the edge. In one shot (#40542) an ELMy (edge localized mode) H-mode subsequently occurs and results in the coexistence of both an internal transport barrier and an edge transport barrier (ETB) until the ramping down of NBI

power. In the other JET shot (#40847), the edge plasma first transits to an ELM-free H-mode and then enters ELMy H-mode phase, during which the internal transport barrier decays. While it is an interesting feature for these two shots that both ITB and ETB coexist, we focus on the ITB behavior in our simulations.

Internal transport barriers are also formed in the two negative central magnetic shear (NCS) discharges in the DIII-D Tokamak,¹⁰ shot #84682 and #87031.^{11,12} NBI is the only auxiliary power source in these two shots, which produced ion temperature profiles with large gradients in the region of the minimum of the q profiles. In the discharge with larger negative central magnetic shear (#84682), the internal transport barrier is steeper than the one in the discharge with weaker NCS (#87031). Both of these DIII-D discharges retain L-mode behavior at the edge, which provides a good opportunity for the study of ITB in the simulations.

The weak and/or reversed magnetic shear in the plasma core is generally considered as an important factor contributing to the formation of ITBs. In the Tokamak Fusion Test Reactor (TFTR)¹³ and DIII-D, internal transport barriers are usually produced with reversed magnetic shear (RS) or negative central magnetic shear in the plasma core. In JET, ITBs occur in the optimized magnetic shear scenario, with low central magnetic shear. One theoretical argument is that the toroidal coupling of the drift modes is weak in regions of low magnetic shear, leaving the modes more slab-like and hence more localized.¹⁴

In addition to the weak or reversed magnetic shear, the $\mathbf{E} \times \mathbf{B}$ flow shear in the core region is considered to be another crucial factor for the formation of ITBs. Since the dis-

^{a)}Also at Institute for Fusion Studies, The University of Texas at Austin, Austin, Texas 78712.

covery of the H-mode, the ion drift mode turbulence suppression due to $\mathbf{E} \times \mathbf{B}$ flow shear has long been identified as the critical mechanism in a number of different high performance regimes.¹⁵ Magnetic shear and $\mathbf{E} \times \mathbf{B}$ flow shear have been incorporated into various transport models, and simulations have been carried out based on a paradigm of the ITB dynamics^{16,17} similar to that of H-mode.^{18,19} In this paradigm, the build-up of the microturbulence level due to the increasing temperature or density gradient driven by auxiliary heating generates spontaneous $\mathbf{E} \times \mathbf{B}$ flow in the plasma through anomalous momentum transport. This is in addition to the $\mathbf{E} \times \mathbf{B}$ flow of plasma that can be driven by input torque (e.g., NBI). The increase in $\mathbf{E} \times \mathbf{B}$ flow shear suppresses the microturbulence, leading to the decrease of anomalous transport of particle and energy and the increase of density and temperature gradients, namely, the formation of the transport barrier. The suppression of the turbulence level also reduces the anomalous driving force (e.g., ‘‘Reynolds stress’’) for the $\mathbf{E} \times \mathbf{B}$ flow and its shear. The balance of these two opposite trends produces a new steady state with higher plasma confinement, which is the case for H-modes when this process happens at the plasma edge. In the central region of plasma, the weak magnetic shear serves as another confinement-enhancing mechanism by reducing the radial decorrelation length of drift modes and decreasing the growth rate of the drift mode ballooning branch. The decrease of the radial correlation length is due to lower density of the rational surfaces.¹⁴ The combination of these two mechanisms, $\mathbf{E} \times \mathbf{B}$ flow and magnetic shear, in the inner region of plasma is expected to result in the formation of ITBs with a power threshold that is lower than if only one mechanism were present. Recently, remarkable agreement with experimental data was reported for the simulations of a DIII-D internal transport barrier discharge by Kinsey *et al.*¹⁷ using the GLF23 transport model.

In our work, we use the Multi-Mode model (MMM) in the time-dependent transport code BALDUR to implement the above ITB paradigm and predictively simulate profiles for the ITBs in the two JET optimized shear (OS) discharges and the two DIII-D negative central shear (NCS) discharges. The Multi-Mode model is an advanced fluid model that is used to compute four channels of transport. This transport model has been used in simulations of a wide range of L-mode and H-mode discharges where good agreement with experimental data is obtained.^{20–22} The $\mathbf{E} \times \mathbf{B}$ flow shear mechanism is implemented in the current version of the Multi-Mode model by subtracting the Hahn–Burrell shearing rate ω_s ,²³ from the drift mode growth rate, or by multiplying the ion drift mode-induced transport coefficients by the suppression factor $1/(1+(Y_s/Y_{sc})^2)$, where Y_s is the Hamaguchi–Horton shear parameter²⁴ (defined in the next section). Both ω_s and Y_s are computed using the radial electric field E_r , which is computed from the poloidal and toroidal flow velocities and the pressure gradient. The poloidal flow velocity is obtained from a neoclassical model,^{25,26} while the toroidal flow velocity is taken from the experimental data. The weak magnetic shear mechanism works through the magnetic shear effect already present in the Weiland model for drift modes in the Multi-Mode model. It also enters the model through the

Hamaguchi–Horton parameter Y_s in combination with the $\mathbf{E} \times \mathbf{B}$ flow shear effect, as noted above. Internal transport barriers are reproduced in our simulations for the discharges in both machines, consistent with the $\mathbf{E} \times \mathbf{B}$ flow shear and weak magnetic shear mechanisms of ITB dynamics.

The paper is organized as follows. In Sec. II, the implementation of $\mathbf{E} \times \mathbf{B}$ flow shear and weak magnetic shear mechanisms in Multi-Mode model are described. Then, in Secs. III and IV the detailed setting for the simulation runs and the corresponding results are presented, respectively. Finally, we summarize the simulation results and discuss possible future work in Sec. V.

II. TRANSPORT MODEL

The Multi-Mode model determines multiple channel anomalous transport coefficients by combining quasilinear transport contributions from several modes that coexist in tokamak plasmas. These include ion temperature gradient (ITG) and trapped electron modes (TEM) in the Weiland model,^{27–29} the drift-Alfvén modes in a model developed by Scott and Bateman,^{30,31} as well as a model for kinetic ballooning modes. A complete description of the model and the parameters in the MMM95 version of the Multi-Mode model is given in Ref. 20. In the current version of the Multi-Mode model, we replace the MMM95 resistive ballooning mode model at the plasma edge with the drift-Alfvén mode model described in Ref. 31. Below, we focus on the implementation of $\mathbf{E} \times \mathbf{B}$ flow shear and magnetic shear stabilization mechanisms in the version of MMM employed in this study.

The $\mathbf{E} \times \mathbf{B}$ flow shear has long been considered as a suppression mechanism for the microturbulence.¹⁵ Gyrokinetic simulations by Waltz *et al.*³² show that the suppression of microturbulence occurs when the Hahn–Burrell $\mathbf{E} \times \mathbf{B}$ flow shearing rate ω_s is greater than the maximum growth rate of all the drift modes. This result is used to simulate the $\mathbf{E} \times \mathbf{B}$ flow shear mechanism in several transport models, including the IFS-PPPL and MMM95 models, by using the reduced growth rate $\gamma - \omega_s$ in the estimation of turbulent transport coefficients. The Hahn–Burrell shearing rate ω_s is given by²³

$$\omega_s = \left| \frac{RB_\theta}{B_\phi} \frac{\partial}{\partial r} \left(\frac{E_r}{RB_\theta} \right) \right|, \quad (1)$$

where the profiles of radial electric field E_r and safety factor q are needed. Here, R is the major radius, B_θ and B_ϕ are poloidal and toroidal components of the magnetic field, respectively, and r is the minor radius (half-width). The radial electric field E_r is usually obtained by solving poloidal and toroidal momentum transport equations for poloidal and toroidal rotation velocity profiles, since

$$E_r = u_{\phi i} B_\theta - u_{\theta i} B_\phi + \frac{1}{Z_i e n_i} \frac{dp_i}{dr}, \quad (2)$$

where $u_{\phi i}$ and $u_{\theta i}$ are, respectively, toroidal and poloidal components of ion velocity, e is the electron charge, Z_i is the ion charge number, n_i is the ion density, and p_i is the ion

pressure. In current BALDUR code, the poloidal rotation velocity $u_{\theta i}$ is computed based on the neoclassical model,^{25,26} while the toroidal rotation velocity $u_{\phi i}$ is taken from experimental measurement, which is available in JET and DIII-D for the impurity ions. The reduced growth rate $\gamma - \omega_s$ is used to compute the turbulent transport coefficients for the drift modes in the Weiland model as one way of implementing the $\mathbf{E} \times \mathbf{B}$ flow shear mechanism in the current Multi-Mode model. However, a coefficient C , greater than unity in front of ω_s in the reduced growth rate $\gamma - C\omega_s$, is required in order to produce simulation profiles that most closely match experimental data in some cases. The need for the coefficient C has been reported by other researchers as well.¹⁷

An alternative to the Hahn–Burrell flow shear model takes into account the effect of weak magnetic shear in addition to the $\mathbf{E} \times \mathbf{B}$ flow shear mechanism. In this model, all the turbulent transport coefficients of ion drift modes are multiplied by a factor $1/[1 + (Y_s/Y_{sc})^2]$, where Y_s is the dimensionless Hamaguchi–Horton shear parameter²⁴

$$Y_s \approx \sqrt{\frac{m_i}{T_e}} \left| \frac{R \partial_{\psi} (E_r / RB_{\theta})}{\partial_{\psi} \ln q} \right|, \quad (3)$$

and Y_{sc} is the critical value ($Y_{sc} \approx 1$). Here, m_i is the ion mass, T_e is the electron temperature, and ψ is the magnetic stream function that can be used to label magnetic surfaces. Note that when the magnetic shear in the denominator in Eq. (3) is small the value of Y_s is greatly increased. In the shear-slab case, Hamaguchi *et al.*²⁴ showed that linear ion temperature gradient mode growth rate decreases as Y_s becomes sufficiently large and that the corresponding turbulent transport is reduced when Y_s rises above a critical value between 1 and 2 in 3D turbulence simulations. These studies suggest the use of Y_s as the $\mathbf{E} \times \mathbf{B}$ flow shear parameter in the weak magnetic shear region and provide the motivation for the above modeling.

The magnetic shear effect enters the Weiland model for drift modes through its influence on the form of the perturbations along the magnetic field lines.²⁸ In the strong magnetic shear region, the electron motions parallel to the magnetic field line are greatly impeded; hence, the perturbations are strongly balloon-like. This ballooning feature of the perturbation is reduced in the weak magnetic shear region, along with the growth rate of the mode. This mechanism is implemented in Weiland model through the averaged ion acoustic operator $\langle \nabla_{\parallel}^2 \rangle$ and the averaged Alfvén operator $\langle \nabla_{\parallel} \nabla_{\perp}^2 \nabla_{\parallel} \rangle$, which are reduced where magnetic shear is weak.

The above transport model is implemented in the time-dependent transport code BALDUR to simulate the formation and evolution of ITBs observed in the JET and DIII-D discharges. The simulations and the results are described in the next two sections.

III. SIMULATION METHODOLOGY

Predictive simulations involve the specification of some of the experimental conditions and the theoretical models. The experimental conditions include:

TABLE I. JET OS and DIII-D NCS discharge parameters.

Shot	JET 40542	JET 40847	DIII-D 84682	DIII-D 87031
Time (s)	47.4	46.9	1.58	1.80
R (m)/ a (m)	2.9/0.94	2.9/0.95	1.7/0.62	1.7/0.65
B_T (T)	3.6	3.6	2.2	2.3
I_p (MA)	3.3	3.2	1.6	1.6
P_{NBI} (MW)	17	19	9.3	9.6
\bar{n}_e (10^{19}m^{-3})	2.5	3.9	2.5	3.1
Working gas	deuterium	deuterium	deuterium	deuterium
Impurity	carbon	carbon	carbon	carbon

- (1) Geometrical and physical parameters: tokamak size, toroidal magnetic field, and properties of the hydrogenic and impurity gases. The parameters for the JET and DIII-D shots are listed in Table I.
- (2) Sources and sinks. In principle, all source profiles should be computed inside the code. In current BALDUR code, NBI power deposition is computed by solving the Fokker–Planck equation based on realistic experimental settings of the beams, while the rf heating power profiles are provided by experimental data. The heating power levels are set according to the experimental data as a function of time. The plasma current ramping in the experiment is followed in the simulations in order to obtain q profiles close to those obtained in the experiments.
- (3) Initial and boundary conditions for density and temperature profiles.

Since the toroidal velocity is not computed in the code, the time evolution of the toroidal rotation profiles are input data needed for the code to compute the radial electric field. All the experimental data are the TRANSP processed data obtained from the International Thermonuclear Experimental Reactor (ITER)³³ Profile Database. The theoretical model includes the following: The 11-equation version of the Weiland model is used for the drift modes in the core.²⁰ The drift-Alfvén mode by Scott and Bateman^{30,31} is taken for the edge mode model. The superset setting of the kinetic ballooning model used in previous MMM simulations is also used here.²⁰ To simulate the favorable effect of plasma elongation, the pressure gradient threshold for the onset of the kinetic ballooning mode is increased from that used for the circular magnetic surface case. This latter choice turns out to be quite important in obtaining the sharp ion temperature gradients in the simulations of the JET discharges.

IV. SIMULATION RESULTS

The experimental and simulation ion temperature profiles at six time slices are shown in Fig. 1 for the two JET discharges and Fig. 2 for the two DIII-D discharges. In the simulations shown in Figs. 1 and 2 the Hahn–Burrell model is employed with a coefficient C as described above. We focus on six time slices of particular interest for each shot.

In the case of JET, the simulations start during the ohmic stage and carry on till the end of all auxiliary heating. The first time slice for the JET discharges is in the middle of the ohmic stage, and the second time slice is right before the

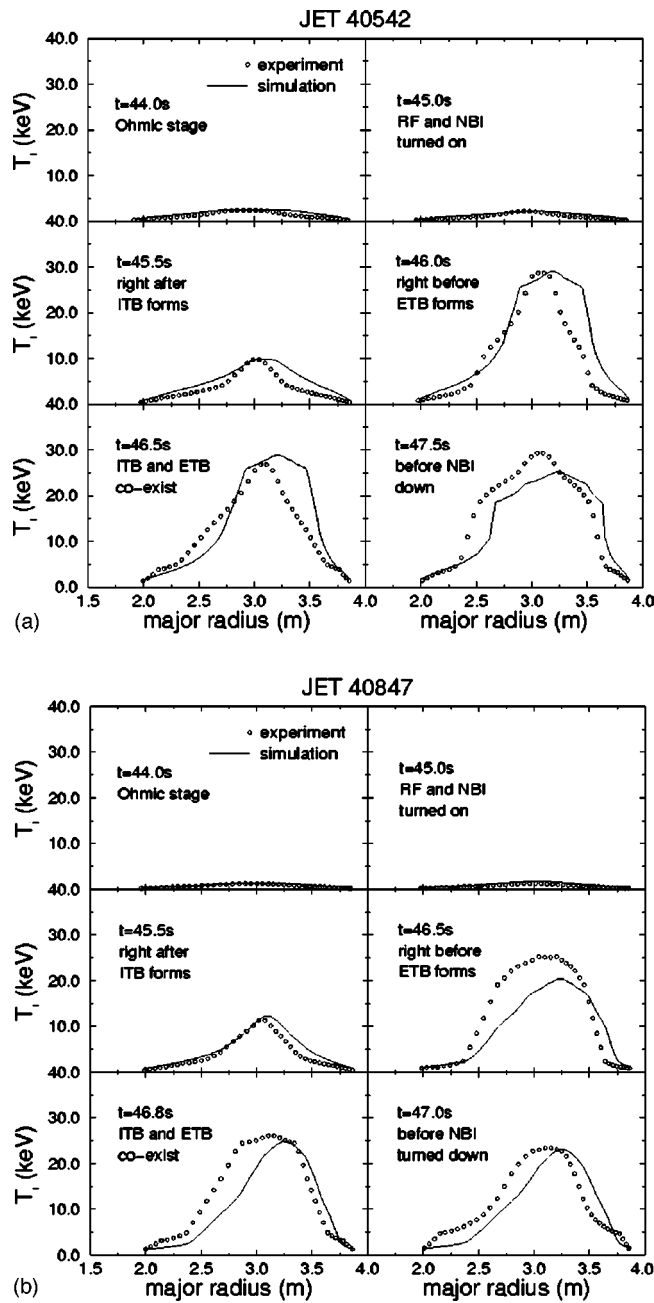


FIG. 1. Experimental ion temperature profiles as a function of major radius (open circles) and the corresponding optimized simulation profiles with Hahm-Burrell flow shear stabilization (solid curves) at six time slices for (a) JET shot #40542, and (b) JET shot #40847.

auxiliary heating is turned on. The third and fourth time slice are taken right after the internal transport barrier forms and just before the formation of the edge transport barrier, respectively. The last two time slices are during the stage when the internal transport barrier coexists with the ELMy H-mode at the edge and before the time when the NBI heating is turned down. In the simulation of the JET discharge #40542, the reduced growth rate $\gamma - \omega_s$ is used for the $\mathbf{E} \times \mathbf{B}$ flow shear mechanism, while in simulation of the JET discharge #40847, a factor $C=3-5$ in front of ω_s is used in the reduced growth rate $\gamma - C\omega_s$ in order to obtain simulated ion temperature profiles in agreement with experiment. Kin-

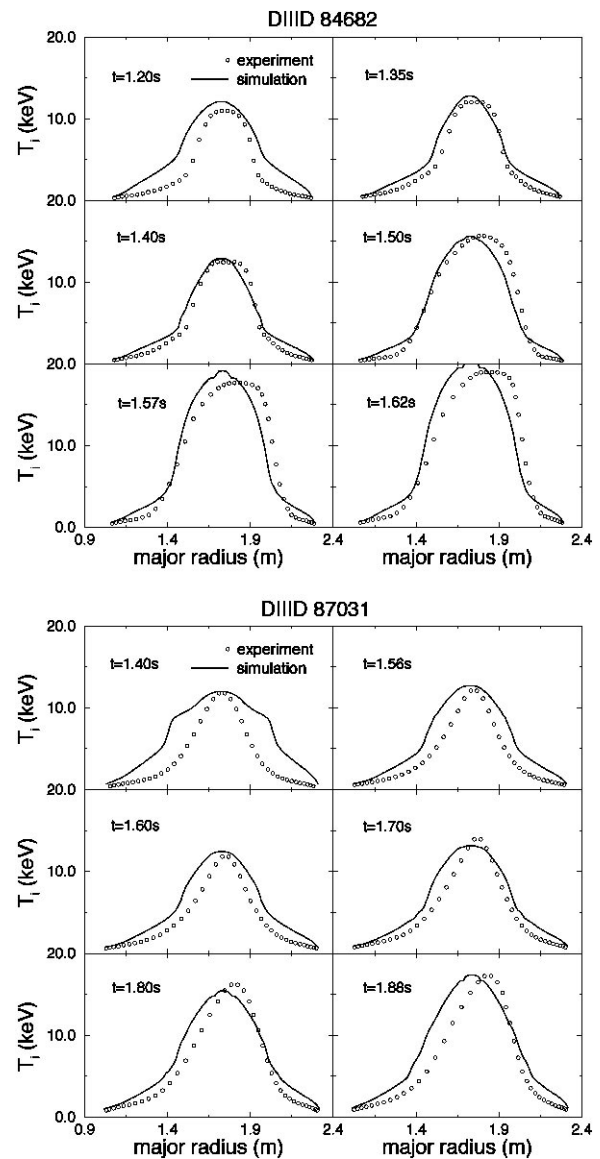


FIG. 2. Experimental ion temperature profiles as a function of major radius (open circles) and the corresponding optimized simulation profiles with Hahm-Burrell flow shear stabilization (solid curves) at six time slices for (a) DIII-D shot #84682, and (b) DIII-D shot #87031.

sey *et al.*¹⁷ found the factor $C=2.65$ is necessary to obtain agreement with the experimental temperature profiles in their simulation of this same JET discharge in which they use the GLF23 transport model. During the early time stages, the times of formation of the ITBs in the simulations for both shots agree with the experimental data. During the evolution of ITBs at later time stages, there are some radial shifts of ITBs in the simulations as compared with the experiments.

In the case of DIII-D, the simulations start at the beginning of the NBI heating stage, where the experimental data are available. In both of the DIII-D discharges, the NBI heating starts with a lower power, and steps up to about double power in the middle of the shot. Plots of the ion temperature profiles at two time slices before, one time slice during, and three time slices after the NBI power step-up are presented. The reduced growth rate $\gamma - \omega_s$ is used for the $\mathbf{E} \times \mathbf{B}$ flow shear mechanism in the simulation of DIII-D shot #84682

and DIII-D shot #87031. The timing and location of the ITBs in the simulations agree well with the experimental data for both shots. Below, we study several aspects of the ITB simulations of both JET and DIII-D shots.

In Sec. IV A below, simulations are presented in more detail for two of the discharges using the Hahn–Burrell flow shear reduction of the growth rate [Eq. (1)] in the Multi-Mode model. For comparison, simulations of the same discharges are presented in Sec. IV B with flow shear stabilization removed from the model. Simulations of the same discharges are presented again in Sec. IV C using the Hamaguchi–Horton flow shear and magnetic shear stabilization model [Eq. (3)]. Finally, statistical analyses of the baseline simulations are presented in Sec. IV D.

A. Dynamic behavior of ITBs

In addition to the evolution of ion temperature radial profiles shown in Figs. 1 and 2, the dynamic behavior of ITBs can also be illustrated by the ion temperature evolution curves at various radii. The experimental and simulation time traces are shown in Fig. 3 for JET shot #40542 and in Fig. 4 for DIII-D shot #84682. In Figs. 3 and 4, each curve represents the ion temperature at a given normalized minor radius as a function of time. In each plot, the curve at the top is the ion temperature trace near the magnetic axis, while the curve at the bottom is the ion temperature trace at the edge of the plasma. The rest of the time traces are at equally spaced intervals of normalized minor radius. Internal transport barriers are characterized by wider spacing between adjacent curves (steeper gradients) relative to the spacing between other adjacent curves.

In the experimental data from the JET shot #40542 [Fig. 3(a)], the time when the ITB first forms is evident from the curves near the inner radii ($t=45.4$ s). At a later time ($t=46.1$ s) the edge transport barrier corresponding to the H-mode is seen from the curves near the plasma edge. In the plot of the simulation data [Fig. 3(b)], the formation of an ITB is seen at $t=45.4$ s, though the formation of an ETB is absent. From Fig. 3(b), it can be seen that the ITB moves from the central region (10 to 27 keV) at $t=46.0$ s to a lower temperature region (9 to 18 keV) at $t=47.5$ s. There is a similar motion in Fig. 3(a) from the central region (especially 20 to 28 keV) at $t=46.0$ s to a region closer to the plasma edge (5 to 17 keV) at $t=47.5$ s. Hence, the simulation shown in Fig. 3(b) follows the trend of the outward radial movement of the ITB observed in the experimental data shown in Fig. 3(a).

In the case of the DIII-D shot #84682, the experimental curves [Fig. 4(a)] show the formation of an ITB at early times (before $t=1.4$ s) and its outward expansion up to $t=1.45$ s. The same trend is also seen in the simulation plot [Fig. 4(b)]. At $t=1.2$ s, the ITB is mostly concentrated between a normalized minor radius of $r/a=0.2$ and $r/a=0.3$ in both the experimental data and the simulation. By $t=1.6$ s, the radial extent of the ITB broadens by extending toward the edge of the plasma, as indicated in both experimental data and in the simulation results.

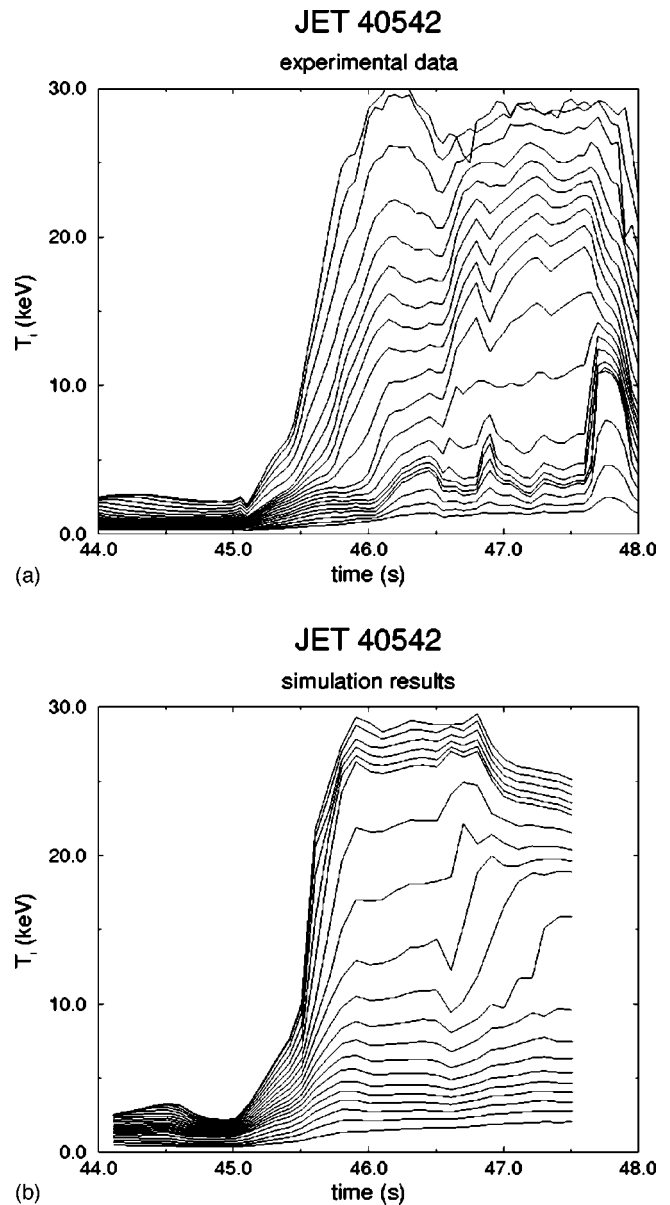


FIG. 3. Ion temperature as function of time at equally spaced intervals in normalized minor radius in (a) experiment, and (b) simulation for JET shot #40542.

B. $\mathbf{E} \times \mathbf{B}$ flow shear effect

In this section, we discuss the comparison of simulations that are carried out *with* and *without* the $\mathbf{E} \times \mathbf{B}$ flow shear effect. In Fig. 5(a), we show the ion thermal diffusivity and, in Fig. 5(b), the ion temperature profiles in simulations for the JET shot #40542 when the $\mathbf{E} \times \mathbf{B}$ flow shear effect is not included in the model. Corresponding results are presented in Figs. 6(a) and 6(b), for DIII-D shot #84682. For both discharges, as seen in Figs. 5(a) and 6(b), the simulation ion temperature profiles are substantially lower than the experimental profiles during the ITB evolution stages. This is particularly the case for the DIII-D discharge. It is seen in Figs. 5(a) and 6(a) that, among all the transport modes, the contribution of the drift modes from the Weiland model to the total ion thermal diffusivity is dominant over most regions of plasma.

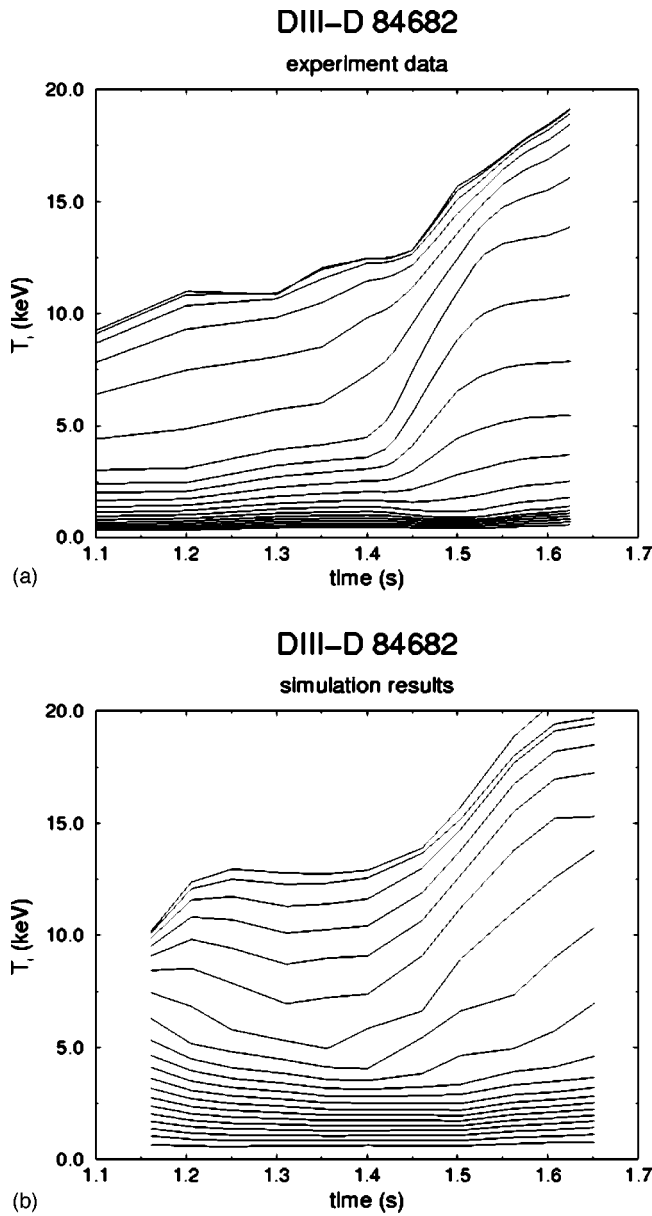


FIG. 4. Ion temperature as function of time at equally spaced intervals in normalized minor radius in (a) experiment, and (b) simulation for DIII-D shot #84682.

When the $\mathbf{E} \times \mathbf{B}$ flow shear effect is included in the model by subtracting the Hahn–Burrell shearing rate ω_s from the growth rates of drift modes, the total ion thermal diffusivity is reduced, and the establishment of the barrier structures become clear. The profiles of Hahn–Burrell shearing rate ω_s in the simulations are plotted in Fig. 7(a) at six time slices for the JET discharge #40542 and in Fig. 8(a) for the DIII-D discharge #84682. The corresponding ion thermal diffusivity and ion temperature profiles after inclusion of ω_s are shown in Figs. 7(b) and 7(c) and in Figs. 8(b) and 8(c). Gaps appear in the ion thermal diffusivity profiles, associated with the steep gradients that form in the ion temperature profiles. It can be seen that the gap and barrier regions occur where the $\mathbf{E} \times \mathbf{B}$ flow shear, ω_s , is maximum in magnitude. The roles of $\mathbf{E} \times \mathbf{B}$ flow shear are apparent when compared with the corresponding cases where the $\mathbf{E} \times \mathbf{B}$ flow

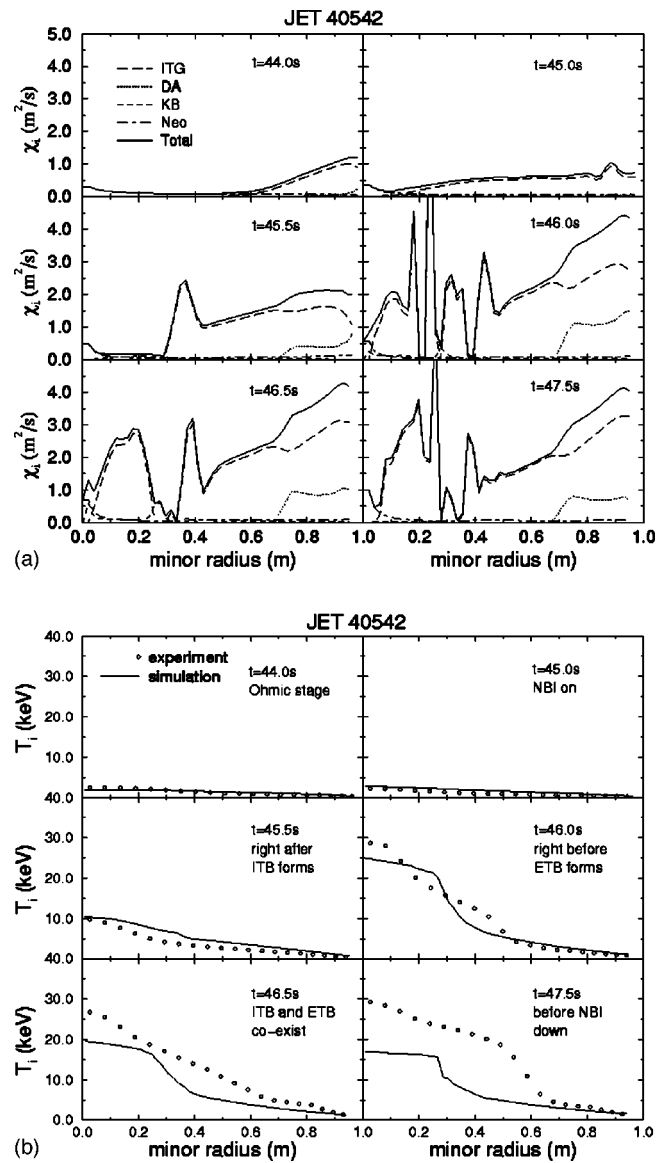
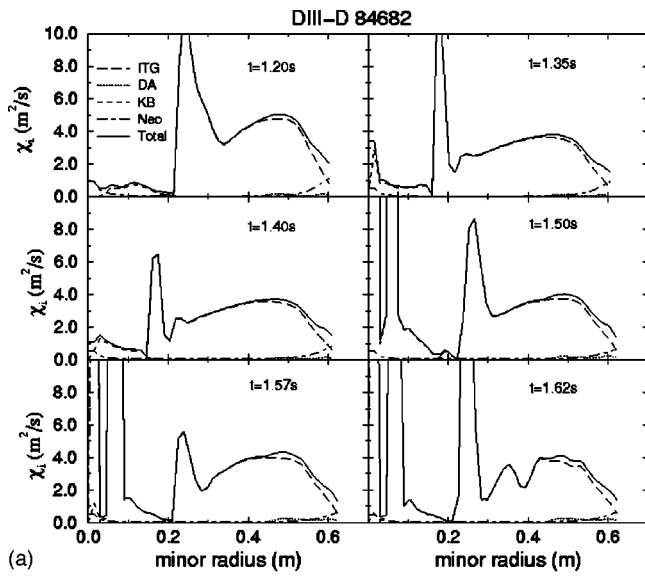


FIG. 5. Profiles as a function of minor radius for the (a) ion thermal diffusivity, and (b) ion temperature from a simulation without $\mathbf{E} \times \mathbf{B}$ flow shear effects for JET shot #40542. In (a), the legend “ITG” stands for diffusivity from drift modes in Weiland model, “DA” for drift-Alfvén mode, “KB” for kinetic ballooning mode, “Neo” for neoclassical diffusivity, and “Total” for total diffusivity.

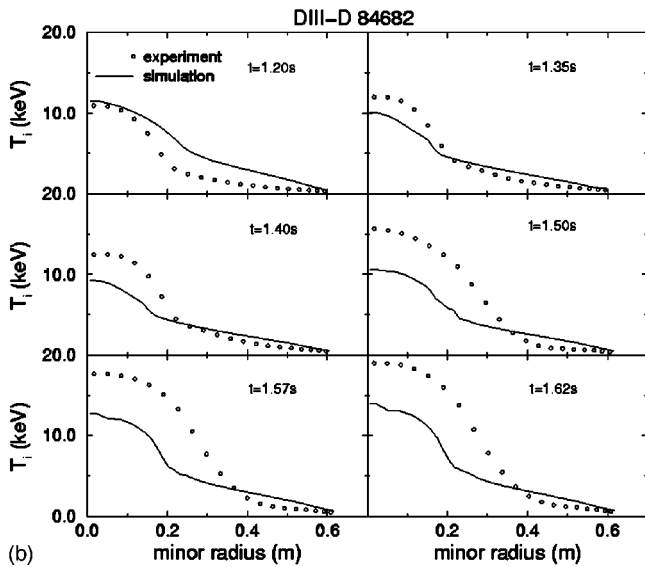
shear effect is absent (Figs. 5 and 6). The $\mathbf{E} \times \mathbf{B}$ flow shear in the DIII-D shot is significantly larger than that in the JET shot, as seen by comparing Figs. 7(a) and 8(a). For this reason, the current implementation of $\mathbf{E} \times \mathbf{B}$ flow shear mechanism seems to be more effective in the simulations of the DIII-D shot than for the JET shot [Figs. 7(c) and 8(c)].

C. Weak magnetic shear and Hamaguchi–Horton parameter Υ_s

The transport simulations shown in this paper predict the time evolution of the magnetic q profile by advancing the magnetic diffusion equation. The optimized magnetic shear feature of the safety factor q profile is well reproduced in the simulation for JET [as illustrated in Fig. 9(a)]. In the DIII-D case, the q profile produced by the simulation has weak cen-



(a)

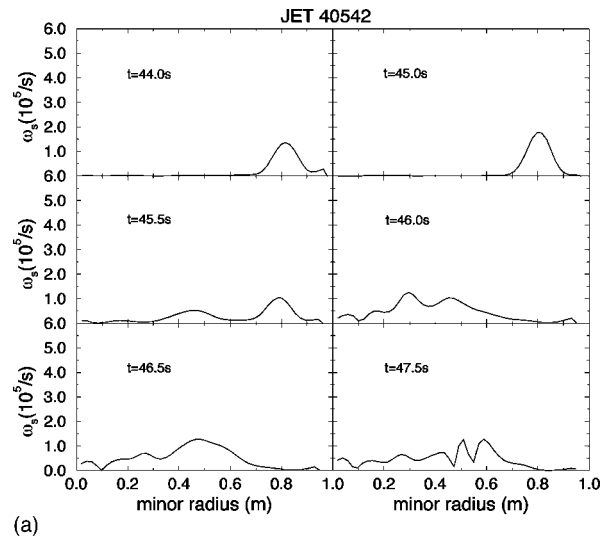


(b)

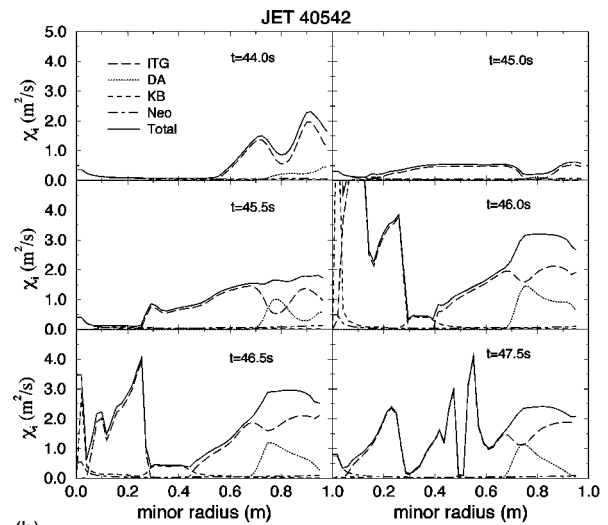
FIG. 6. Profiles as a function of minor radius for the (a) ion thermal diffusivity, and (b) ion temperature from a simulation without $\mathbf{E} \times \mathbf{B}$ flow shear effects for DIII-D shot #84682. In (a), the legend ITG stands for diffusivity from drift modes in Weiland model, DA for drift-Alfvén mode, KB for kinetic ballooning mode, Neo for neoclassical diffusivity, and Total for total diffusivity.

tral magnetic shear instead of the negative central magnetic shear in experiment [Fig. 9(b)]. However, in our transport model, it is the (weak) magnitude of magnetic shear that is significant, while the sign of the shear is irrelevant. Therefore, the q profile with weak shear in the simulation does produce the transport effect of the q profile with negative magnetic shear in our transport model for DIII-D, since both the simulation and the experimental q profiles have similar weak shear at the central region.

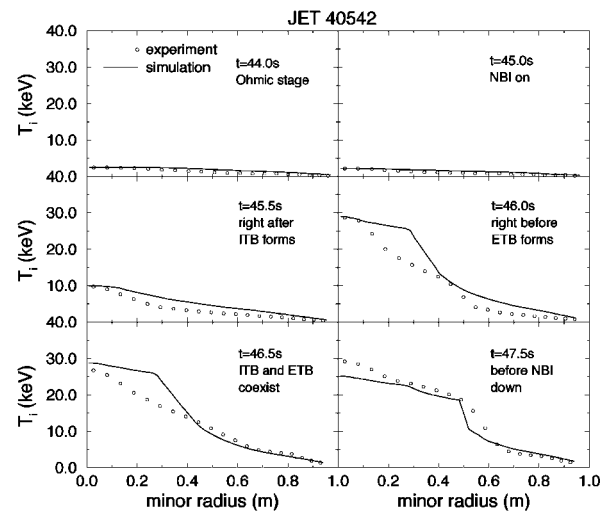
Here, the alternative implementation of $\mathbf{E} \times \mathbf{B}$ flow shear mechanism that includes weak magnetic shear effects through the Hamaguchi–Horton shear parameter Y_s [Eq. (3)] is examined. The value of Y_s is plotted in Fig. 10(a) for JET shot #40542 and in Fig. 11(a) for DIII-D shot #84682. We see Y_s profiles are peaked at both the maximum $\mathbf{E} \times \mathbf{B}$ flow



(a)



(b)



(c)

FIG. 7. Profiles as a function of minor radius for the (a) Hahn–Burrell $\mathbf{E} \times \mathbf{B}$ flow shearing rate ω_s , (b) ion thermal diffusivity, and (c) ion temperature from a simulation with Hahn–Burrell $\mathbf{E} \times \mathbf{B}$ flow shear effects for JET shot #40542. In (b), the legend ITG stands for diffusivity from drift modes in Weiland model, DA for drift-Alfvén mode, KB for kinetic ballooning mode, Neo for neoclassical diffusivity, and Total for total diffusivity.

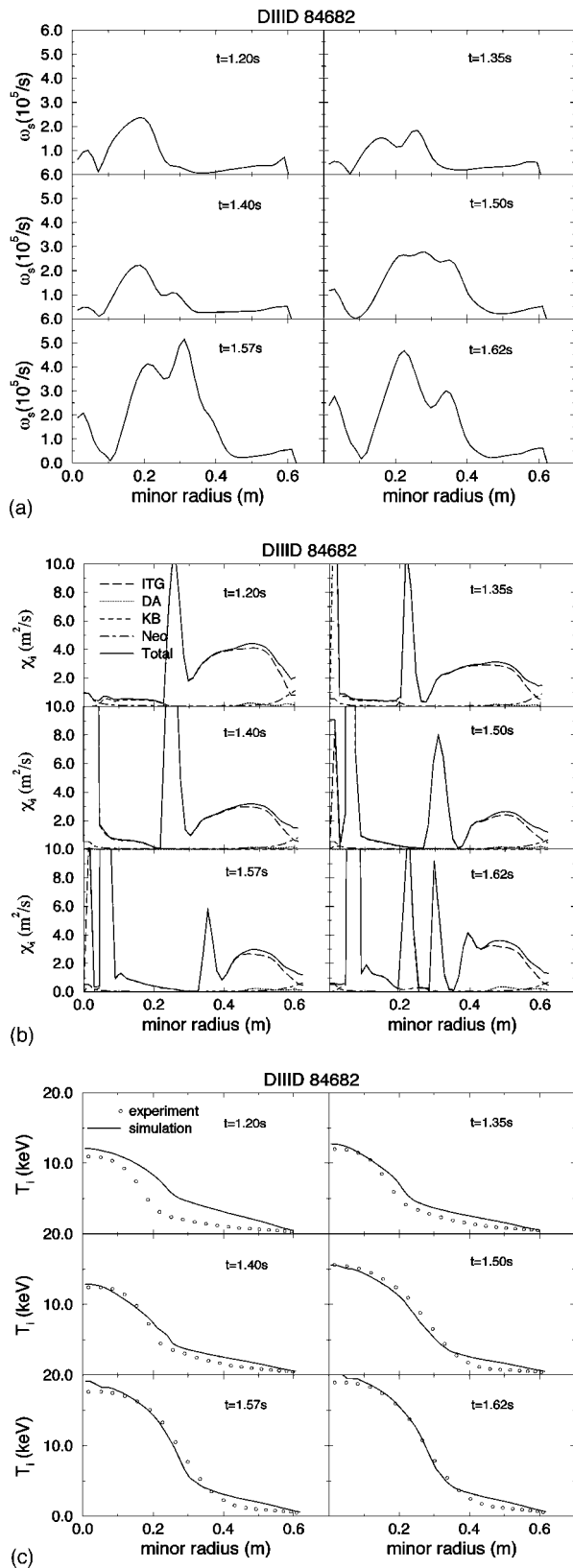


FIG. 8. Profiles as a function of minor radius for the (a) Hahn-Burrell $E \times B$ flow shearing rate ω_s , (b) ion thermal diffusivity, and (c) ion temperature from a simulation with Hahn-Burrell $E \times B$ flow shear effects for DIII-D shot #84682. In (b), the legend ITG stands for diffusivity from drift modes in Weiland model, DA for drift-Alfvén mode, KB for kinetic ballooning mode, Neo for neoclassical diffusivity, and Total for total diffusivity.

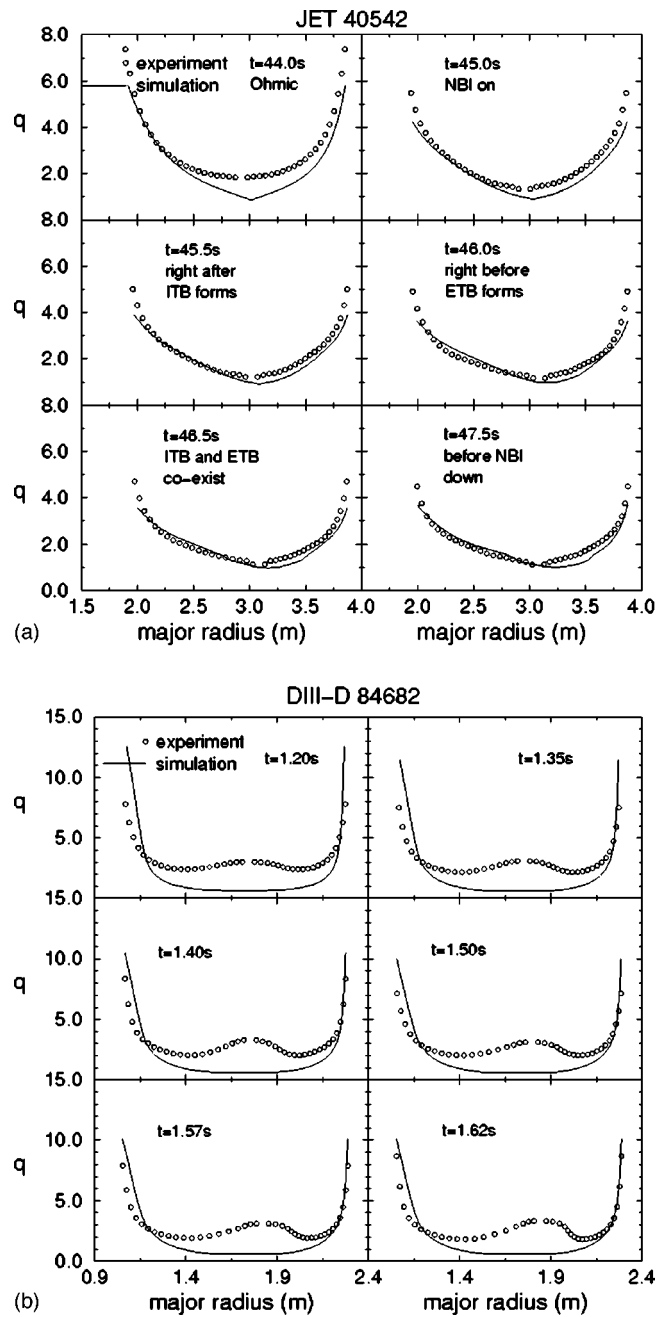
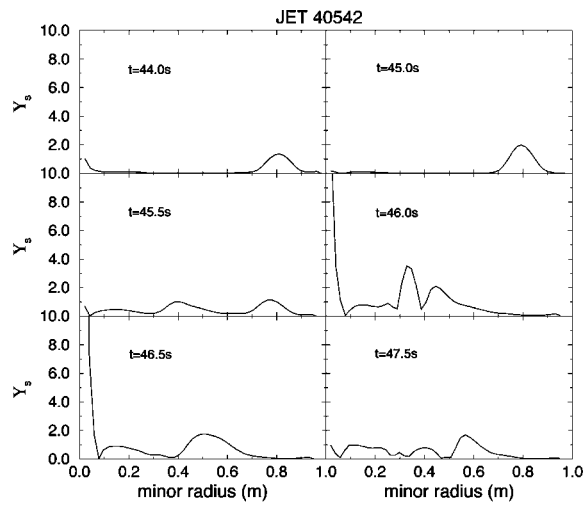
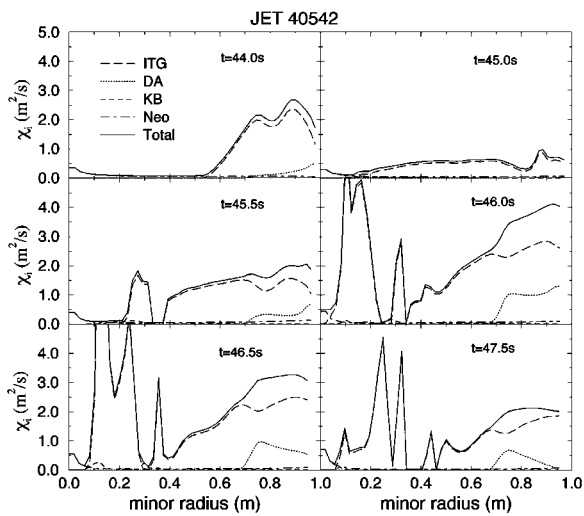


FIG. 9. Experimental safety factor q profiles (open circles) at six time slices and the corresponding simulation profiles (solid curves) for a) JET shot #40542, and (b) DIII-D shot #84682.

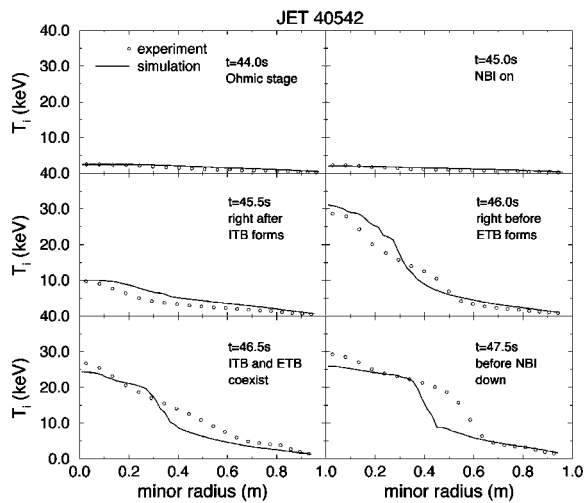
shear rate ω_s and the low central magnetic shear regions in cases of both shots. In Figs. 10(b) and 11(b) we see the reduction of the thermal diffusivity χ_i by Y_s , especially in the central region of plasma. Transport barriers are also reproduced in ion temperature profiles of the simulations, where the agreement with experiment depends on the choice of the critical value Y_{sc} . In particular, $Y_{sc} = 1$ is used for the JET case in Fig. 10 and $Y_{sc} = 0.5$ is used for the DIII-D case in Fig. 11. In general, the ion temperature profiles of the simulations using this model tend to be narrowly peaked in the inner plasma. In the DIII-D case, the values of Y_s are much greater than that in the JET case, due to the nearly zero magnetic shear over the broader central region of plasma and



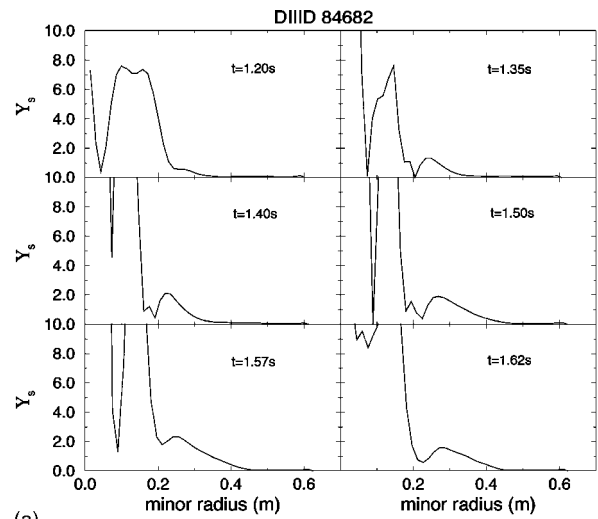
(a)



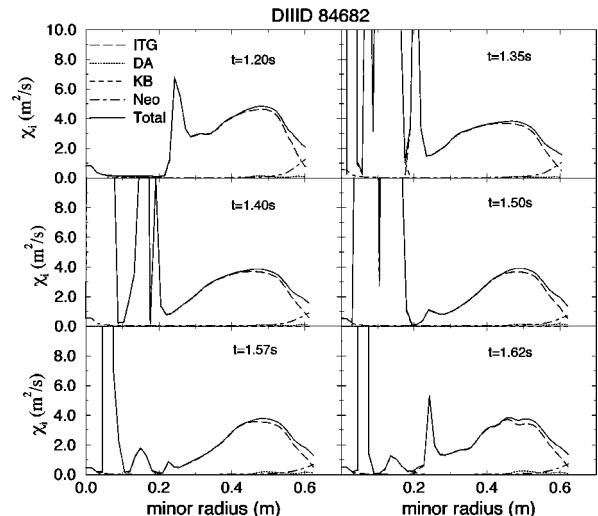
(b)



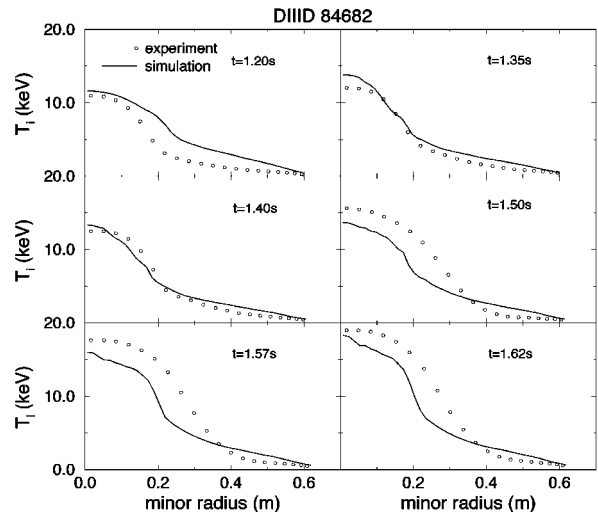
(c)



(a)



(b)



(c)

FIG. 10. Profiles as a function of minor radius for the (a) Hamaguchi-Horton $E \times B$ flow shear parameter Y_s , (b) ion thermal diffusivity, and (c) ion temperature from a simulation with Hamaguchi-Horton $E \times B$ flow shear effects for JET shot #40542. In (b), the legend ITG stands for diffusivity from drift modes in Weiland model, DA for drift-Alfvén mode, KB for kinetic ballooning mode, Neo for neoclassical diffusivity, and Total for total diffusivity.

FIG. 11. Profiles as a function of minor radius for the (a) Hamaguchi-Horton $E \times B$ flow shear parameter Y_s , (b) ion thermal diffusivity, and (c) ion temperature from a simulation with Hamaguchi-Horton $E \times B$ flow shear effects for DIII-D shot #84682. In (b), the legend ITG stands for diffusivity from drift modes in Weiland model, DA for drift-Alfvén mode, KB for kinetic ballooning mode, Neo for neoclassical diffusivity, and Total for total diffusivity.

TABLE II. Simulation statistics for JET simulations.

JET 40542				JET 40847			
Time (s)	σ_{T_i} (%)	σ_{T_e} (%)	σ_{N_e} (%)	Time (s)	σ_{T_i} (%)	σ_{T_e} (%)	σ_{N_e} (%)
44.0	22	39	7	44.0	12	18	10
45.0	19	30	9	45.0	26	11	7
45.5	19	13	9	45.5	12	11	6
46.0	20	12	11	46.5	19	12	14
46.5	20	17	11	46.8	17	13	16
47.5	16	20	11	47.0	16	13	12

stronger $\mathbf{E} \times \mathbf{B}$ flow shear in DIII-D barrier region [Figs. 10(a) and 11(a)]. Hence, the flow and magnetic shear have more influence on the ion thermal diffusivity and temperature profiles in the simulations of DIII-D than in the corresponding simulations of JET.

D. Statistical analysis of the simulations

To quantify the comparison of simulations with experiments, we compute the relative root-mean-square (rms) deviation between the two profiles for the six time slices of the four discharges we simulated. In this paper, the relative rms deviation of each quantity X (T_i , T_e , and n_e) is defined as

$$\sigma_X = \sqrt{\frac{1}{N} \sum_{j=1}^N \left(\frac{X_j^{\text{exp}} - X_j^{\text{sim}}}{X_{\text{max}}^{\text{exp}}} \right)^2}, \quad (4)$$

where X_j^{exp} is the j th data point of the experimental profile, X_j^{sim} is the corresponding data point of the simulation profile, and $X_{\text{max}}^{\text{exp}}$ is the maximum data point of the experimental profile of X as a function of radius, which has N points in total. We list the relative rms deviations of ion temperature T_i , electron temperature T_e , and electron density n_e , which are denoted as σ_{T_i} , σ_{T_e} , and σ_{n_e} , respectively, in Table II for the two JET discharges, and in Table III for the two DIII-D discharges.

For the JET simulations, the statistics show that the simulation profiles generally match the experimental data about equally well during all the auxiliary heating stages of the discharges. During these time stages with transport barriers, the relative rms deviations are within 20%, which is

comparable with the general experimental measurement error. In the DIII-D cases, the overall relative rms deviations are smaller than for the JET cases.

V. SUMMARY AND DISCUSSION

In the Multi-Mode model that we used here, the overall mechanisms of the ITB dynamics are implemented in three different levels: theoretical, empirical, and experimental. The theoretical models include the Weiland model for ion drift modes, the Scott and Bateman model for drift-Alfvén mode at the plasma edge, and the neoclassical model for the poloidal plasma flow. The kinetic ballooning mode model and the $\mathbf{E} \times \mathbf{B}$ flow shear mechanism are implemented empirically. The toroidal velocity profiles from experimental data have been used directly instead of predicting toroidal velocity with a toroidal momentum transport model.

Simulations carried out with this transport model have reproduced the internal transport barriers observed in both JET OS and DIII-D NCS discharges. For the two JET shots, the exact location of the ITB differs from the location indicated by experimental data at later time stages after the barrier first occurs. For the two DIII-D shots, the timing and location of ITBs in the simulations agree with the experimental results. From the effects of $\mathbf{E} \times \mathbf{B}$ flow shear and q profile on the profiles of ion thermal diffusivity and ion temperature, we interpret the formation of internal transport barrier as resulting from the combined effects of $\mathbf{E} \times \mathbf{B}$ flow shear and the weak magnetic shear configuration. We considered two implementations of $\mathbf{E} \times \mathbf{B}$ flow shear mechanism: (1) ion drift mode growth rate is reduced by Hahn–Burrell $\mathbf{E} \times \mathbf{B}$ flow shearing rate, and (2) ion drift mode-induced transport coefficients are reduced by a suppression factor

TABLE III. Simulation statistics for DIII-D simulations.

DIII-D 84682				DIII-D 87031			
Time (s)	σ_{T_i} (%)	σ_{T_e} (%)	σ_{N_e} (%)	Time (s)	σ_{T_i} (%)	σ_{T_e} (%)	σ_{N_e} (%)
1.20	20	24	18	1.40	26	17	10
1.35	9	14	6	1.56	17	10	10
1.40	7	15	6	1.60	14	9	10
1.50	10	21	9	1.70	10	14	12
1.57	13	21	13	1.80	9	12	14
1.62	13	19	17	1.88	12	12	18

$1/(1+(Y_s/Y_{sc})^2)$, where Y_s is the Hamaguchi–Horton shear parameter. For the simulations presented, these two methods yield similar results.

Future efforts will be aimed at reducing or eliminating elements of empiricism in parts of the transport model used in this paper. It is found that the simulations are particularly sensitive to the kinetic ballooning mode model settings. Future work will include the development of a better model for the kinetic ballooning mode.^{31,34,35} A drift mode model that intrinsically includes the $\mathbf{E} \times \mathbf{B}$ flow shear effects might remove the uncertainty of the multiplier in front of the shear parameter ω_s or in the parameter Y_s . Also, it would be desirable to implement a toroidal momentum transport model that self-consistently computes the toroidal velocity profiles, instead of relying on experimental data. The toroidal momentum transport equation requires input torque and the anomalous viscosity, which would result in the requirement for additional improvements in other packages of the transport code. It is likely that the electron temperature profiles predicted by simulations would be in better agreement with experimental data when the transport model is extended to include a proper treatment of the electron temperature gradient (ETG) mode, which affects the electron transport channel. In both of the JET discharges simulated in this paper, the edge transport barriers due to ELMy H-modes are not predicted in the simulations, since the current model used in our simulations does not include the ELMy H-mode physics. The implementation of a proper edge model will also be addressed in future work.

ACKNOWLEDGMENTS

We are grateful to Dr. V. V. Parail and Dr. J. E. Kinsey for providing the JET and the DIII-D experimental data. This work was supported by the U.S. Department of Energy Contracts No. DE-FG02-92-ER-54141 and No. DE-FG03-96ER-54346.

¹Y. Koide, M. Kikuchi, M. Mori *et al.*, Phys. Rev. Lett. **72**, 3662 (1994).

²M. Mori, S. Ishida, T. Ando *et al.*, Nucl. Fusion **34**, 1045 (1994).

³F. Levinton, M. Zarnstorff, S. Batha *et al.*, Phys. Rev. Lett. **75**, 4417 (1995).

⁴E. Strait, L. Lao, M. Mauel *et al.*, Phys. Rev. Lett. **75**, 4421 (1995).

⁵C. Gormezano and the JET Team, in *Proceedings of the Sixteenth International Atomic Energy Agency Fusion Energy Conference, Montréal, Canada, 1996* (International Atomic Energy Agency, Vienna, 1997), Vol. 1, p. 487.

⁶F. Soldner and the JET Team, Plasma Phys. Controlled Fusion **39**, B353 (1997).

⁷H. Ninomiya and the JT-60 Team, Phys. Fluids B **4**, 2070 (1992).

⁸P.-H. Rebut, R. J. Bickerton, and B. E. Keen, Nucl. Fusion **25**, 1011 (1985).

⁹V. Parail, Y. Baranov, C. Challis *et al.*, Nucl. Fusion **39**, 429 (1999).

¹⁰J. L. Luxon and L. G. Davis, Fusion Technol. **8**, 441 (1985).

¹¹B. W. Rice, E. A. Lazarus, M. E. Austin *et al.*, Nucl. Fusion **36**, 1271 (1996).

¹²D. Schissel, C. M. Greenfield, J. C. Deboo *et al.*, in Ref. 5, Vol. 1, p. 463, Paper IAEA F1-CN-64/A5-3.

¹³D. J. Grove and D. M. Meade, Nucl. Fusion **25**, 1167 (1985).

¹⁴A. Beklemishev and W. Horton, Phys. Fluids B **4**, 2176 (1992).

¹⁵H. Biglari, P. H. Diamond, and P. W. Terry, Phys. Fluids B **2**, 1 (1990).

¹⁶A. Fukuyama, K. Itoh, S.-I. Itoh, and M. Yagi, in *Proceedings of the Seventeenth International Atomic Energy Agency Fusion Energy Conference, Yokohama, Japan, 19–24 October, 1998* (International Atomic Energy Agency, Vienna, 1999), p. 1367.

¹⁷J. E. Kinsey, R. E. Waltz, G. M. Staebler, and H. S. John, in *European Physical Society Meeting, Maastricht, Netherlands June 1999* (European Physical Society, Petit-Lancy, Switzerland, 2000).

¹⁸H. Sugama and W. Horton, Phys. Plasmas **2**, 2989 (1995).

¹⁹P. Diamond, V. Lebedev, D. Newman, B. Carreras, T. Hahm, W. Tang, G. Rewoldt, and K. Avinash, Phys. Rev. Lett. **78**, 1472 (1997).

²⁰G. Bateman, A. H. Kritiz, J. E. Kinsey, A. J. Redd, and J. Weiland, Phys. Plasmas **5**, 1793 (1998).

²¹J. E. Kinsey, Nucl. Fusion **39**, 539 (1999).

²²G. Bateman, J. E. Kinsey, A. H. Kritiz, A. J. Redd, and J. Weiland, in *Proceedings of the Sixteenth International Atomic Energy Agency Fusion Energy Conference, Montréal, Canada, 7–11 October* (International Atomic Energy Agency, Vienna, 1996), Vol. II, pp. 559–565.

²³T. S. Hahm and K. H. Burrell, Phys. Plasmas **2**, 1648 (1995).

²⁴S. Hamaguchi and W. Horton, Phys. Fluids B **4**, 319 (1992).

²⁵D. Ernst, M. Bell, R. Bell *et al.*, Phys. Plasmas **5**, 665 (1998).

²⁶P. Zhu, W. Horton, and H. Sugama, Phys. Plasmas **6**, 2503 (1999).

²⁷H. Nordman, J. Weiland, and A. Jarmén, Nucl. Fusion **30**, 983 (1990).

²⁸J. Weiland and A. Hirose, Nucl. Fusion **32**, 151 (1992).

²⁹J. Nilsson and J. Weiland, Nucl. Fusion **34**, 803 (1994).

³⁰B. Scott, Plasma Phys. Controlled Fusion **39**, 1635 (1997).

³¹G. Bateman, A. H. Kritiz, A. J. Redd, M. Erba, G. Rewoldt, J. Weiland, P. Strand, J. E. Kinsey, and B. Scott, in *Proceedings of the Seventeenth International Atomic Energy Agency Fusion Energy Conference, Yokohama, Japan, 19–24 October, 1998* (International Atomic Energy Agency, Vienna, 1999), p. 1569.

³²R. E. Waltz, G. D. Kerbel, J. Milovich, and G. W. Hammett, Phys. Plasmas **1**, 2229 (1994).

³³R. Aymar, V. Chuyanov, M. Huguet, R. Parker, and Y. Shimomura, in Ref. 5, Vol. 1, pp. 3–18.

³⁴A. J. Redd, “Pressure-driven transport in the core of tokamak plasmas,” Ph.D. thesis, Lehigh University, Bethlehem, PA (1998).

³⁵B. Hong, W. Horton, and D.-I. Choi, Plasma Phys. Controlled Fusion **31**, 1291 (1989).